Graphene nanoribbons: fabrication, properties and devices

Arlenciu Celis, Maya N. Nair, Amina Taleb - Ibrahimi, Edward H Conrad, Claire Berger, Walt de Heer, Antonio Tejeda

HAL Id: hal-01403647

https://hal.science/hal-01403647

Submitted on 26 Nov 2016

Graphene nanoribbons: fabrication, properties and devices

You may also be interested in:

Guide Through the Nanocarbon Jungle: Guide Through the Nanocarbon Jungle
D Tománek

The role of defects and doping in 2D graphene sheets and 1D nanoribbons
Humberto Terrones, Ruitao Lv, Mauricio Terrones et al.

Structured epitaxial graphene: growth and properties
Yike Hu, Ming Ruan, Zelei Guo et al.

Electronic properties of graphene: a perspective from scanning tunneling microscopy and magnetotransport
Eva Y Andrei, Guohong Li and Xu Du

Nature of Graphene Edges: A Review
Muge Acik and Yves J. Chabal

Transport through graphene quantum dots
J Güttinger, F Molitor, C Stampfer et al.

Thermoelectric effects in graphene nanostructures
Philippe Dollfus, Viet Hung Nguyen and Jérôme Saint-Martin

Topical Review

Graphene nanoribbons: fabrication, properties and devices

A Celis[1,2]**, M N Nair**[2]**, A Taleb-Ibrahimi**[2]**, E H Conrad**[3]**, C Berger**[3,4]**,
W A de Heer**[4] **and A Tejeda**[1,2]

[1] Laboratoire de Physique des Solides, CNRS, Université Paris-Sud, Université Paris-Saclay, 91405 Orsay, France
[2] Synchrotron SOLEIL/UR1 CNRS, Saint-Aubin, 91192 Gif-sur-Yvette, France
[3] The Georgia Institute of Technology, Atlanta, GA 30332-0430, USA
[4] Institut Néel CNRS - Université Grenoble, Alpes, Grenoble, 38042, France

E-mail: antonio.tejeda@u-psud.fr

CrossMark

Abstract

Graphene nanoribbons are fundamental components to the development of graphene nanoelectronics. At the nanoscale, electronic confinement effects and electronic edge states become essential to the properties of graphene. These effects depend critically on the ribbon width and the nature of the ribbon edge, the control of which at the atomic scale is a major challenge. Graphene nanoribbons have been largely studied theoretically, experimentally and with the perspective of electronic applications. We review the basic properties of graphene nanoribbons and recent progress in fabrication processes, focusing on the question of the electronic gap. We examine top–down and bottom–up approaches to fabricate graphene nanoribbons by lithographic, catalytic cutting, chemical assembly and epitaxial growth methods and compare their electronic characteristics.

Keywords: graphene, nanoribbon, fabrication, devices

(Some figures may appear in colour only in the online journal)

1. Introduction

Electronic devices have become our everyday companions. They are everywhere in our lives since miniaturization has allowed extremely powerful devices to be portable. Miniaturization itself was made possible thanks to the development of nanoelectronics. Graphene's unique combination of properties has attracted attention for electronic applications [1]. It is patternable, scalable and has demonstrated high mobility and even room temperature ballistic transport [2]. However, graphene is gapless and cannot be used as such in digital electronics that need large current on/off ratios. Therefore a great deal of effort has been directed towards opening a band gap in graphene without significantly affecting its mobility. Strain can in principle open a gap [3–5] but

the uniaxial strain to produce useful gaps for electronics is extremely high and not realistically achievable. Chemical methods have also been proposed, based on doping or functionalization by an atom or a molecule [6–17]. Doping leading to gaps as large as 1 eV and hydrogenation up to ∼700 meV were reported [7–10]. Because of the nature of the chemical grafting process, disorder is almost inevitable, which leads to a significant degradation of the mobility.

A particularly elegant method to open a band gap is electronic confinement [1]. The importance of electronic confinement on the electronic properties of graphene was realized very early on in magnetotransport experiments [18]. For certain graphene ribbons of a few nm in width, theory predicts that the band gap varies as a function of the ribbon width W [19, 20] with $\Delta E(W) \sim 1\,\text{eV·nm}\,W^{-1}$. This means that a band

gap of $\sim$100 meV is expected for a ribbon of 10 nm, or conversely, a ribbon of width $\sim$1 nm would be required to get the band gap of silicon ($\sim$1 eV).

As quantum confinement only relies on the geometric structure of the ribbon, the band gap can in principle be varied by design, contrary to the fixed band gap of a semiconductor-like silicon. This, together with graphene's high mobility and high-current-carrying capabilities, has motivated a large number of studies of graphene nanoribbons that we review in this article. We will focus more particularly on the question of the gap opening in nanoribbons. We will see in particular that well-defined nanostructures are required with predictable, reliable and scalable fabrication methods and how techniques like epitaxial graphene sidewall nanoribbons on SiC meet these criteria. After this introduction, the section 2 presents the electronic and magnetic properties of ideal isolated graphene nanoribbons as predicted by theory. The section 3 focuses on the fabrication methods and some of the resulting physical properties characteristic of each process. We review in section 4 a common aspect to all the preparations: edge states and the edge stability. We then examine in section 5 more practical aspects including transport, transistors and heterojunctions. We finish the review with brief conclusions and perspectives.

2. Electronic structure of ideal graphene nanoribbons: calculations

Ideal ribbons with simple edge orientation and termination, of extremely narrow width, and isolated from any substrate influence have been extensively studied. Simple edge termination is defined by the orientation of the ribbon respectively to the graphene lattice. Due to their high symmetry, the most studied graphene nanoribbons are those with zigzag and armchair edges. Zigzag ribbons have a honeycomb network oriented in such a way that the edge is made of the triangular edges of the hexagons (figure 1(a)-top left). Armchair ribbons are oriented at 30° (or equivalently at 90°) from the zigzag orientation. In this case, the edge is made of hexagonal sides (figure 1(a)-top right). All other ordered orientations are chiral.

Early tight-binding calculations [19, 20] have shown that the band structure of narrow ribbons depends on their orientation. Specifically, in these calculations, zigzag ribbons are always metallic (figure 1(b)) and armchair ribbons present an alternance of metallic and gapped electronic structures depending on the width. When present, the gap scales inversely with the ribbon's width. In figure 1(b), the calculated bands are projected either along the direction defined by the lattice parameter $\boldsymbol{a}$ (parallel to the armchair direction) or along $\boldsymbol{z}$ (parallel to the zigzag direction) (figure 1(a)-bottom). With this convention, $k = \pi$ corresponds to the k point where the Brillouin zone edge is reached along $\boldsymbol{a}^*$ or $\boldsymbol{z}^*$ reciprocal vectors, respectively [19] (figure 1(a)-bottom). The width is characterized by N carbon dimer lines, which are different for armchair or zigzag ribbons, as presented in figure 1(a)-top. The electronic structures for different values of N are shown in figure 1(b). Explicitly, the ribbon is metallic for $N = 3M - 1$, where M is an integer, and presents a gap otherwize. More

recent *ab initio* calculations have confirmed the presence of a significant band gap in all 1 nm to $\sim$4 nm wide armchair ribbons, with a gap value that decreases with width and oscillates with N [21, 23–27] (figure 1(d)).

The situation is qualitatively different for zigzag ribbons, for which tight-binding calculations find a flat band at zero energy (highlighted by the box in figure 1(b)) that corresponds to states that are located at the edge of the ribbons. These edge states produce a peak in the DOS at the Fermi level, enhancing the temperature dependence of their paramagnetic susceptibility.

In the case of zigzag ribbons, first-principle calculations have shown that the flat band of the high DOS at zero energy found in simple tight-binding calculations is unstable relative to spin splitting. Magnetic ordering is predicted on the edges of narrow zigzag ribbons, with long-range ferromagnetic polarization along each edge and anti-ferromagnetism across the ribbon of the edge states [20, 28, 29]. Therefore very close to charge neutrality, the electronic conductance is favoured for one spin direction, which may have implications for spintronics. Half-metallicity is also proposed [22] by applying an in-plane electric field to modify the natural energy distribution of spins in the ribbon. This results in a single type of spin state at the Fermi level, as shown in figure 1(d). Another peculiarity of zigzag ribbons is that a perfectly conducting channel was predicted in tight-binding models, even in the presence of long-range impurity scattering [30]. This is because at charge neutrality, backscattering requires a band of inverse dispersion dE/dk which is not present at the same K point in the Brillouin zone. This perfectly conducting channel is also predicted for chiral (non-armchair) ribbons. Exceptional transport properties are therefore predicted for zigzag or chiral ribbons with perfect edges.

All these predicted properties strongly rely however on an atomic control of the width (smaller than a few nm) and of the edges of ribbons. It is thus extremely important to produce high-quality ribbons to obtain well-defined physical properties. In the following, we report the most common methods to produce graphene nanoribbons.

3. Fabrication methods and related electronic properties

Graphene nanoribbons can be synthesized by top–down or bottom–up approaches. The top–down approach consists of modifying a large graphene sheet (i.e. patterning) until a desired nanometric size and shape is reached. The bottom–up approach consists of assembling small building blocks to construct the desired larger object. In addition to these two common methods for building nanostructures, we will describe an original approach to obtain sidewall nanoribbons which combines both the top–down (lithography) and bottom–up (epitaxial growth) processes.

3.1. Top–down approaches

3.1.1. Lithographic patterning methods. Graphene nanoribbons can be fabricated by standard lithography and etching
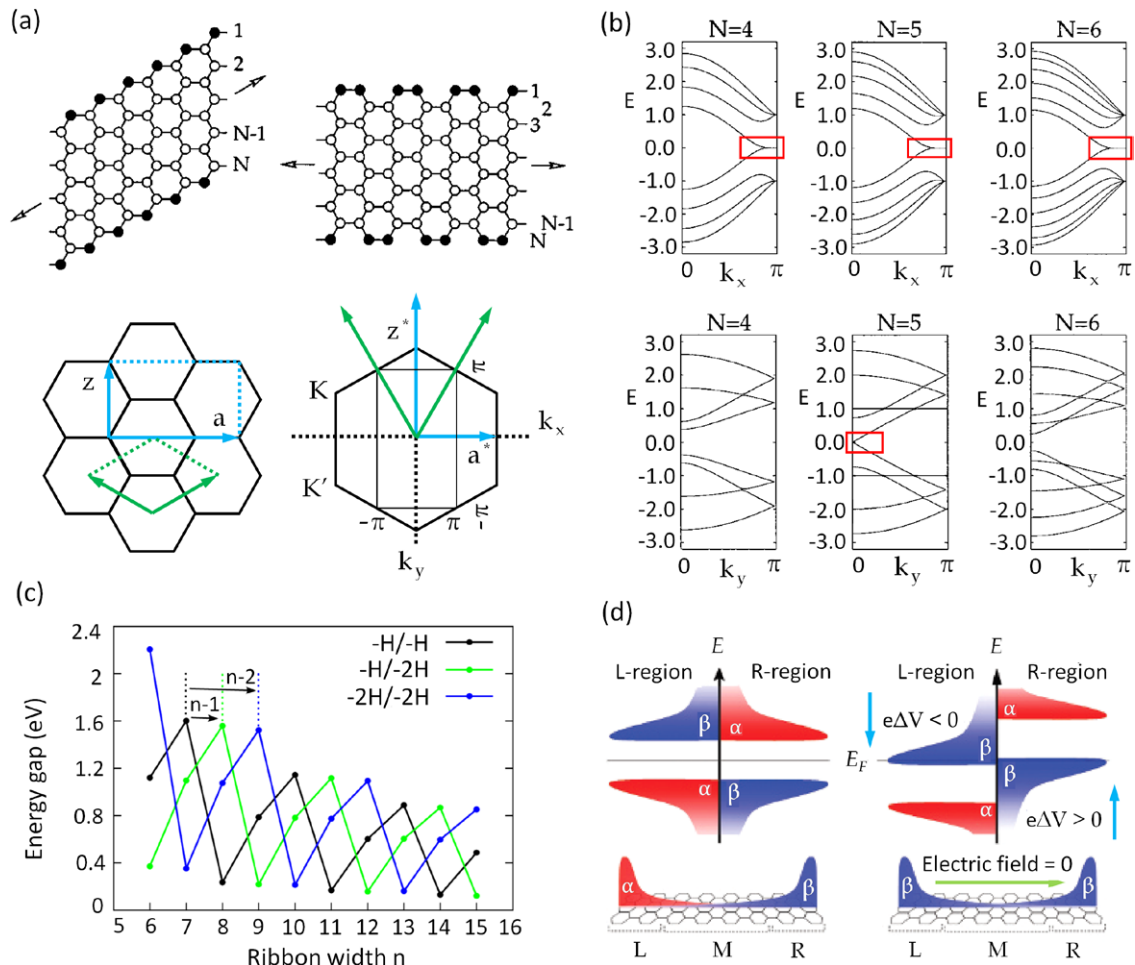
Figure 1. Theoretical properties of graphene nanoribbons. (a) Top: representation of a zigzag (left) and armchair nanoribbon (right). The arrows indicate the long direction of the ribbons. Bottom: schematic indicating the direction where the electronic structure in (b) was calculated. The left panel is the real space representing graphene and the right panel is its reciprocal space. The rectangular unit cell for calculations is defined by **a** and **z**. (b) Electronic band structure calculated by tight-binding for various graphene nanoribbon widths ($N = 4, 5, 6$, as defined in (a)). Top row: zigzag nanoribbons have a metallic state at $E = 0$. Bottom row: armchair nanoribbons exhibit either metallic or semiconducting behaviours, depending on the presence of an edge state at E_F (metallic states in the red box). The band gap is width-dependent [19]. Reprinted figure with permission from Nakada *et al* [19]. Copyright 2015 by the American Physical Society. (c) Density functional theory (DFT) calculations showing an oscillation of the band gap as a function of the ribbon width in functionalized armchair nanoribbons [21]. Reprinted with permission from Wagner *et al* [21]. Copyright 2013 by the American Chemical Society. (d) *ab initio* calculation of the spin-resolved density of states (DOS) (top) and local DOS (bottom) of zigzag nanoribbons in the absence of an electric field (left). In the presence of a transverse electric field (right), the band at E_F is single spin-polarized [22]. Reprinted with permission from Macmillan Publishers Ltd: Nature 444, 347, copyright 2006.

techniques of exfoliated graphene flakes; graphene grown on metals by chemical vapor deposition (CVD) or epitaxial graphene on SiC. For this a mask is lithographically patterned on a graphene sheet so that graphene can be etched away by an oxygen plasma everywhere except for the strip protected by the mask [1, 31, 32, 35–43]. Ribbons have been obtained with a minimum width down to about 10 nm [44, 45].

Figure 2(a) shows the schematic process for a nanowire mask and the resulting ribbons as imaged by a STM, after the mask was removed. Figure 2(b) shows SEM and cross-sectional TEM image of an array of ~10 nm wide nanoribbons. In this image the polymer mask was not removed for a better imaging of the spacing between the ribbons. The edge quality at an atomic level is better viewed in a STM. Figure 2(c) shows a STM image of a different ribbon obtained by e-beam lithography of epitaxial graphene on SiC. The edge has a

nanometric corrugation that shows disorder, indicating how difficult it is to obtain pure zigzag or armchair edge types. A zoom of the image in the rectangle (figure 2(c) right) reveals the mixture of armchair and zigzag edges as highlighted by the superposition of the green graphene honeycomb structure. Rough edges come from the difficulty of patterning a resist with an electron beam at the atomic level, but also from the instability in the plasma etching process. Smooth and well-defined edges and ribbon width have not been demonstrated in lithographically-patterned graphene, although recent progress was made [45], and relatively high mobilities are reported $3500 \, cm^2(V \cdot s)^{-1}$ [50].

Local probes not only allow direct observation of the quality of the edges, but they can also be used to etch material, and ribbon edges have been tailored with TEM, a STM and atomic force microscope (AFM). STM lithography has produced
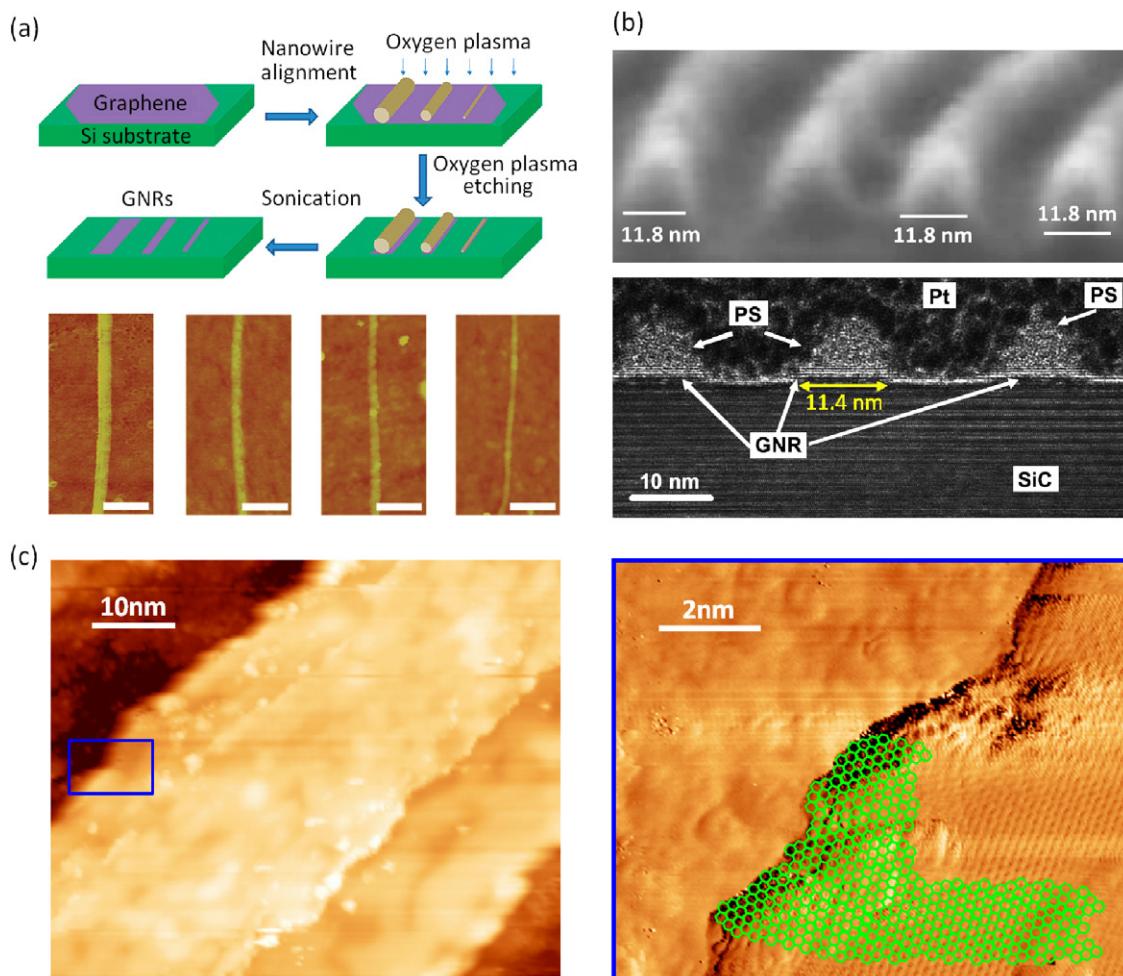
Figure 2. Lithographic ribbons. (a) Oxygen-plasma-patterned graphene nanoribbons with a nanowire protecting mask. Top panel: graphene is deposited on a substrate and nanowires are placed on top. An oxygen plasma etches away the unprotected graphene. The wires are removed and the nanoribbons are revealed on the substrate. Bottom panel: scanning tunnelling microscope (STM) image of these nanoribbons [31]. Adapted with permission from Bai *et al* [31]. Copyright 2009 by the American Chemical Society. (b) Microscopy images of lithographically-patterned graphene ribbons. Top panel: scanning electron microscopy (SEM) image showing the nanoribbon covered with the etching mask resist. Bottom panel: cross-sectional transmission electron microscopy (TEM) image showing the ribbons with the resist mask on top [32]. Adapted with permission from Liu *et al* [32]. Copyright 2012 by the American Chemical Society. (c) E-beam lithographically-patterned graphene nanoribbons on SiC. Overall topography of the ribbon as seen by a STM (left) and zoom on the edge (rectangle) showing atomic resolution (right).

sub-10 nm nanoribbons cut out of HOPG along a desired crystallographic direction by applying high voltages to etch carbon away [33, 51]. AFM heated tips were used to locally deoxidize multilayer epitaxial graphene oxide to reduce it locally to graphene [52]; ribbon widths down to 12 nm were realized this way. AFM can be used on any kind of substrate and is therefore very versatile at producing nanostructures that can be directly measured [52]. Figure 3(a)-left shows a nanoribbon initially etched in HOPH with a STM tip to obtain an overall armchair direction. The etch direction was then rotated by 30° to obtain a zigzag direction. Figure 3(a)-right shows the degree of control that can be reached with this technique: the overall orientation can be selected with a nanometric precision although a significant edge disorder still remains due to the etching procedure. The lithographic principle is similar in TEM. Here energetic electron beams (>80 keV) can tailor ribbons down to width of 0.7 nm [34]. Figure 3(b) shows a nanoribbon of hundreds of nm width tailored in this way

from a suspended graphene flake. These images indicate that although these techniques are extremely local, control of the edge structure at the atomic level remains a challenge. Moreover, these techniques are not well adapted for the large-scale production of graphene nanoribbons. 'Millipede' microscopes could in principle use over 1000 tips for improving fabrication by parallel production [33].

3.1.2. Chemical methods. Chemical reactions give a high degree of control over the production of large quantities of graphene nanoribbons with a defined size distribution. In appropriate solutions, graphitic precursors (graphite or carbon-based molecules) can undergo chemical reactions that produce graphene nanoribbons in a powder or in a dispersed solution (figure 4(a) [46, 53–55], with a ribbon size distribution centred around a specific value ⩾1 nm. However, the ribbons are usually organized in a network, as shown by TEM in figure 4(b). It is possible to characterize individual
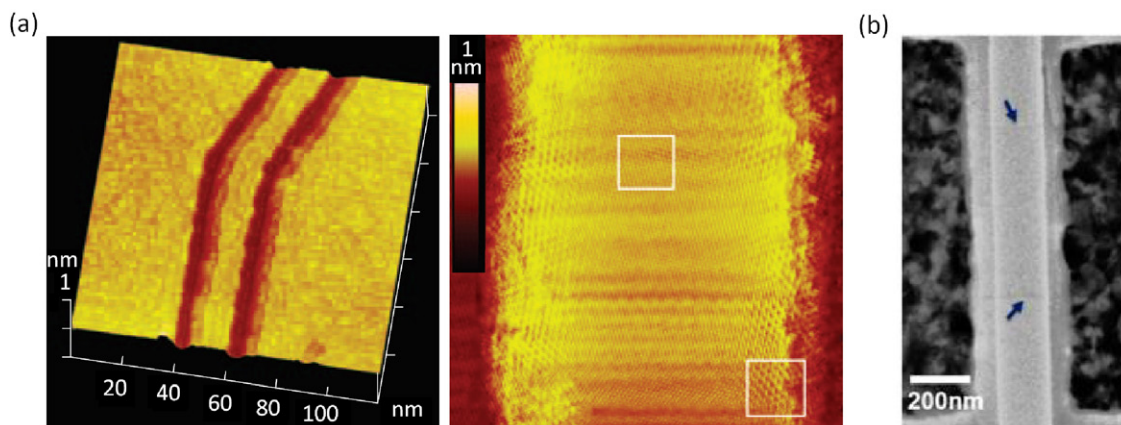
Figure 3. Local probe lithographic ribbons. (a) STM lithographic nanoribbons cut in highly-oriented pyrolitic graphite (HOPG). Left: STM image of a continuous nanoribbon with overall armchair and zigzag direction due to 30° change in the etching direction. Right: atomic resolution on the ribbon [33]. Reprinted with permission from Macmillan Publishers Ltd: Nature Nanotechnology 3, 397. Copyright 2008. (b) TEM lithographic graphene nanoribbons. The arrows show the ribbon limits from suspended graphene [34]. Reprinted with permission from Qi *et al* [34]. Copyright 2014 by the American Chemical Society.
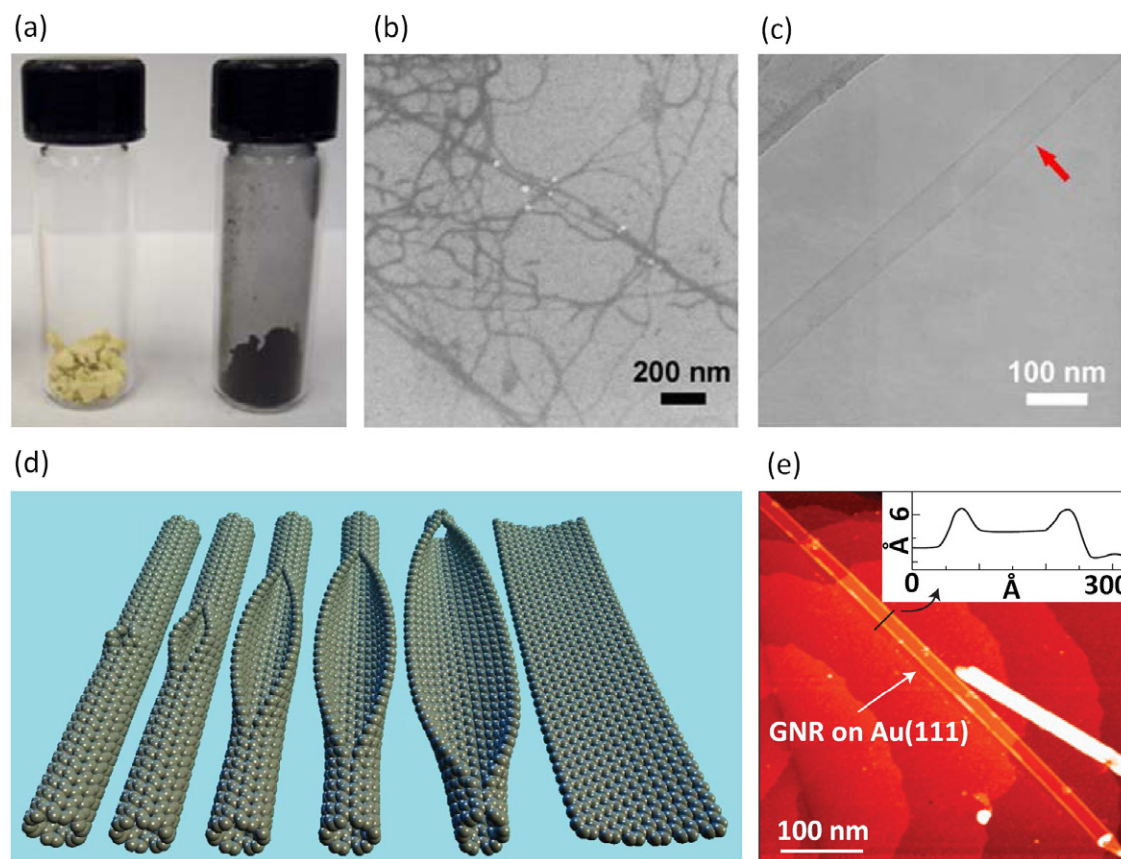

Figure 4. Graphene nanoribbons obtained by chemical methods. (a) Yellow precursor and final black graphene nanoribbon powder [46]. Reprinted with permission from Macmillan Publishers Ltd: Nature Communications, 5, 3189. Copyright 2014. (b) SEM image of graphene nanoribbons dispersed in solution exhibiting a web-like structure. (c) TEM image of a single nanoribbon. The arrow points to a ~ 60 nm wide nanoribbon [47]. (d) A schematic of the unzipping process of single wall carbon nanotubes (SWCNTs) into nanoribbons by chemical agents [48]. Reprinted by permission from Macmillan Publishers Ltd: Nature 458, 872. Copyright 2009. (e) STM image of unzipped carbon nanotube (CNT) deposited on Au(1 1 1). The inset shows the cross-sectional profile of the resulting ribbon [49] (reprinted with permission from Macmillan Publishers Ltd: Nature Physics 7, 613. Copyright 2011.

nanoribbons, as in figure 4(c). The reported mobilities for this type of synthesis utilising time-resolved THz spectroscopy for ribbons dispersed in the liquid phase are within the range 150–$15\,000\,\text{cm}^2\,(\text{V}\cdot\text{s})^{-1}$ [56, 57].

Another chemical method exploits SWCNTs or multi-wall CNTs as graphitic precursors. These precursors are dispersed in solution with specific chemical agents that cause their walls to unzip. The unzipping process is schematically described in
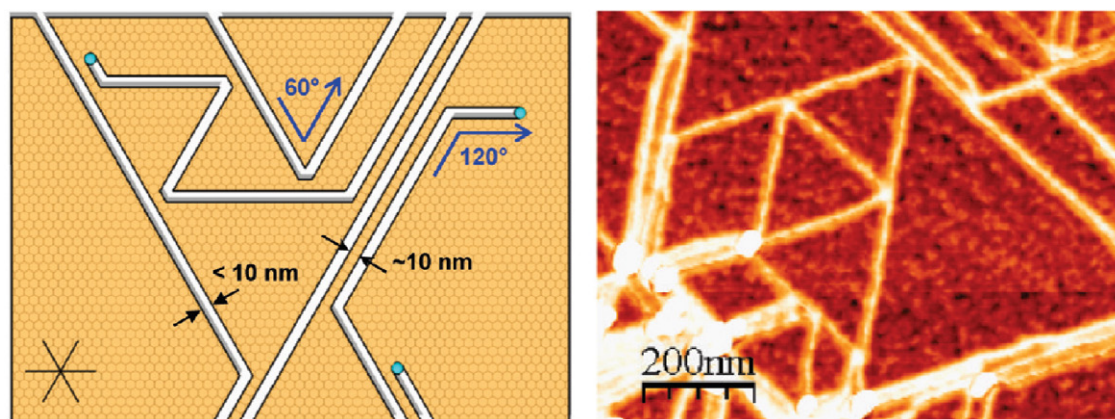
Figure 5. Graphene nanoribbon obtained by cutting with catalytic particles. Left: Model of paths made by metallic particles when cutting graphene by a catalytic reaction. Nanoribbons can be as narrow as 10 nm and display preferential zigzag edges. Right: AFM phase contrast image, showing the resulting patterns that include ribbons, triangles and rhombus [63]. Adapted with permission from Campos *et al* [63]. Copyright 2009 by the American Chemical Society.

figure 4(d). Selected nanoribbons are probed by a STM on a Au(1 1 1) substrate as shown in figure 4(e). The width distribution, length and single/multiple layer character depend to a great extent on the initial CNT (diameter, single/multi-wall ratio of the processing batch and overall quality) [48, 57–62].

3.1.3. Graphene cutting with catalytic particles. Carbon-carbon bonds can be dissociated via a catalytical reaction. This is put to use to cut out graphene nanostructures from a graphene flake by depositing particles of a catalytic metal. In particular, metallic particles such as Fe or Ni interact with graphene in the presence of a hydrogen atmosphere and dissociate carbon-carbon bonds. This interaction etches the graphene while producing gas products composed of C and H, such as CH_4. Nanoribbons can be produced when the cutting paths of the particles run parallel to each other rather than cross, creating graphene nanoribbons as narrow as 10 nm with well-defined edges [63–65].

The directionality of the cutting paths is well-defined, as shown by the schematic (figure 5(a)) of the AFM image of a graphene surface exposed to metallic particles (figure 5(b)). However the cutting directions cannot be predetermined so that a wide variety of graphene nanostructure shapes are obtained. If this technique is to lead to applications, further experimental work will be needed to control the nanoribbon shapes.

3.2. Bottom–up approaches

3.2.1. Molecular precursor-based growth. In this process, graphene nanoribbons are formed out of monomeric precursors that react at the surface of catalytic metals. Monomers like DBBA (10,10'-dibromo-9,9'-bianthryl) or its derivatives are sublimated onto a slightly hot metallic surface (∼200 °C) to stimulate the production of polymeric chains. A subsequent higher temperature annealing (∼400 °C) favours the dehydrogenation of the polymer chains, resulting in graphene nanoribbons, as shown by a STM (figure 6(a)) [66]. A variant consists of a room temperature deposition before annealing [69].

Photoemission experiments on aligned parallel ribbons allow their electronic properties to be probed with *k* resolution. Figure 6(b) shows the electronic states of an armchair graphene nanoribbon at Γ, with a binding energy as large as 1 eV and with a low dispersion, indicating the localized nature of the spectral feature. A detailed analysis of the spectral weight reveals two components as expected from calculations [67], indicated in the figure by the two curved lines. Complementary information can be obtained by a STM, as local spectroscopy reveals the presence of 'end states' located where the edge locally changes from armchair to zigzag (figure 6(c)) [68]. All these studies show that while molecular precursor-based growth is restricted to metallic substrates, they provide a fruitful playground for fundamental studies of graphene nanoribbons.

3.2.2. CVD. CVD can be used to generate graphene nanoribbons in a similar way to molecular precursor-based growth but in a single step. In this case a metallic template serves as the catalyst for the decomposition of hydrocarbons like ethylene (C_2H_4) or methane (CH_4) at high temperature (700–1000 °C). Graphene forms by the assembly of the carbon atoms once the C-H bonds are broken. Depending on the catalytic template, the resulting nanoribbons vary in size [70–73]. Figure 7(a) describes the process for the nanoribbons growth. A Ni nanobar template is first evaporated onto a SiO_2/Si substrate. The substrate is then exposed to ethylene at high temperature, seeding the growth of the graphene nanoribbon at the nanobar. The precision of the size and shape of the nanoribbon is only limited by the ability to create proper templates. The SEM image of figure 7(b) shows an example of a nanoribbon grown on Ni nanobars of various sizes connected to two electrodes. Note that the ribbon is sitting on a Ni template, and transfer methods are required for transport measurements.

3.3. Epitaxial graphene on SiC sidewall growth

So far we have reviewed both bottom–up and top–down approaches. In the following, we describe the growth of
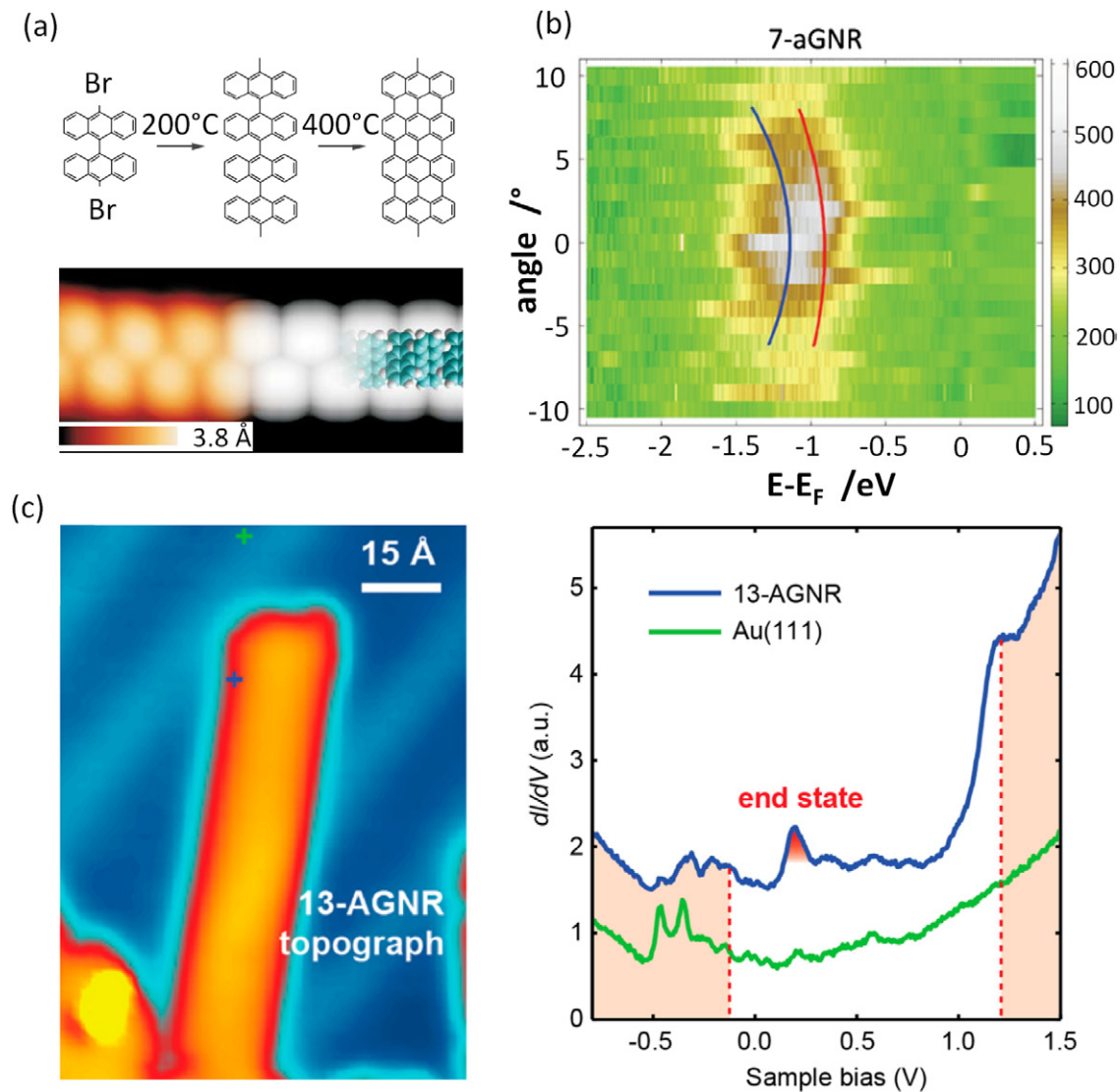
Figure 6. Molecular precursor-based nanoribbons. (a) Polymeric chain assembly reaction for DBBA molecules (top panel). STM image of the resulting armchair graphene nanoribbon (bottom panel) [66] (reprinted with permission from Macmillan Publishers Ltd: Nature 466, 470. Copyright 2010. (b) Electronic states of armchair graphene nanoribbons in the direction along the ribbon [67]. Reprinted figure with permission from Linden *et al* [67]. Copyright 2012 by the American Physical Society. (c) STM image of an armchair nanoribbon (left) and the d*I*/d*V* spectra on the edge (right), taken at the crosses in the left image [68]. Reprinted with permission from Chen *et al* [68]. Copyright 2013 by the American Chemical Society.

sidewall epitaxial graphene nanoribbons, that combine both approaches by exploiting lithography and epitaxial growth. When heated in a vacuum or in an inert atmosphere SiC decomposes by silicon sublimation. The remaining carbon atoms rearrange as a graphene layer [1, 75]. Epitaxial graphene on SiC was chosen from the start for developing graphene electronics [1] because graphene is directly produced on a semiconducting single crystal wafer. Contrary to the methods presented above there is no need to transfer to another substrate and large area epitaxial graphene is ready for surface science investigation and transport measurements.

As seen above it is generally a challenge to combine nanoribbons' growth only at a desired location while controlling the ribbon direction and ribbon edge smoothness directly on an insulating substrate. Sprinkle *et al* [78] developed a technique that solves these problems. This consists of the epitaxial

growth of sidewall nanoribbons on crystalline 4H/6H-silicon carbide wafers. For this, artificial trenches are etched at predetermined locations on the 4H/6H-SiC (0 0 0 1)- face (the Si-terminated face). By high-temperature annealing the trench sidewalls crystallize via SiC step flow into stable SiC facets onto which graphene grows selectively. The ribbon width is determined by the trench depth that can be tuned very reliably by SiC plasma etching. These sidewall ribbons have smooth edges that merge into SiC or into the graphene layer that is bound to SiC (buffer layer).

Growth models of graphene on stepped SiC have been proposed (figure 8(a)) [74, 79, 80]. Silicon atoms sublimate preferentially at the SiC steps and the remaining C atoms form a graphene layer. This layer extends first towards the upper flat surface (plateau). To test this model in sidewall ribbons, we have analysed a facet annealed under the
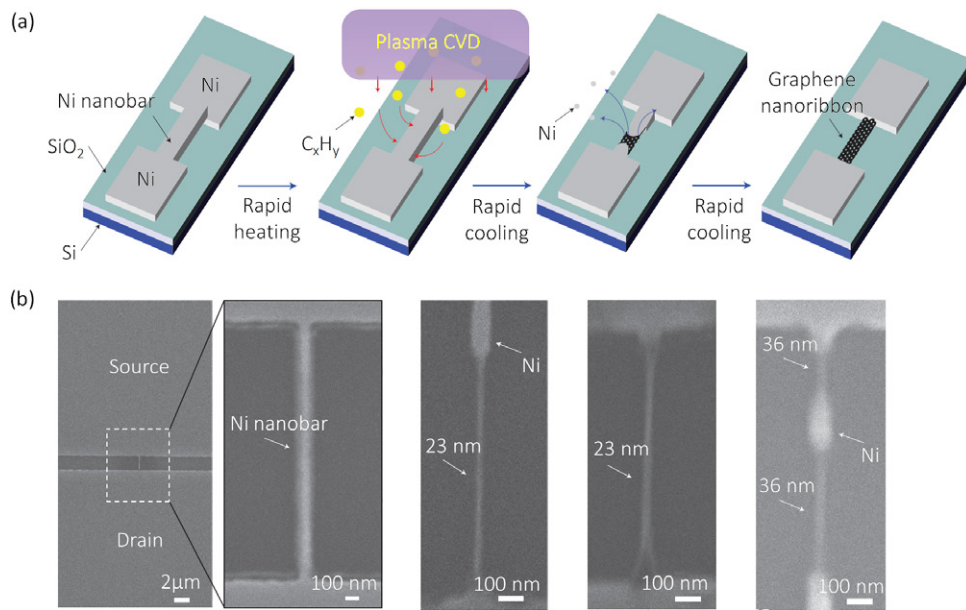
Figure 7. CVD ribbons. (a) Schematic of the CVD process to fabricate graphene nanoribbons by using Ni nanobars. From left to right: a Ni nanobar template is deposited on top of a substrate. Ethylene (C_2H_4) is exposed to the hot surface, where it reacts by catalysis with the Ni. Graphene is seeded on the bar until it covers it, generating a graphene nanoribbon. (b) SEM images of resulting nanoribbons with different sizes on the Ni template [70]. Reprinted with permission from Macmillan Publishers Ltd: Nature Nanotechnology 7, 651. Copyright 2012.
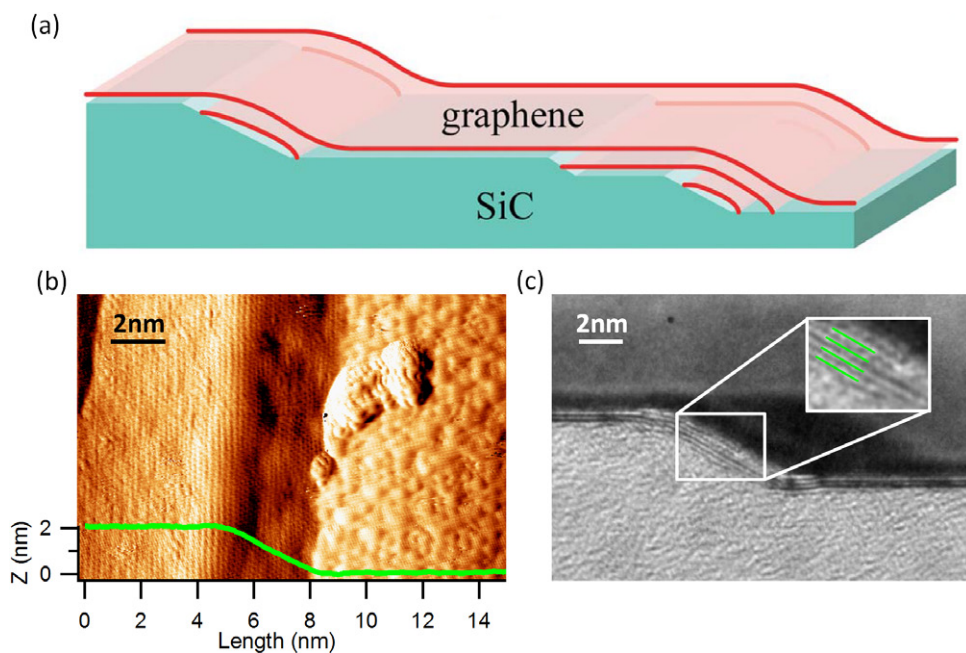

Figure 8. Growth of epitaxial graphene sidewall ribbons on SiC. (a) Schematic of growth mechanism of graphene on SiC [74]. Reprinted from Physica E: Low-dimensional Systems and Nanostructures vol. 42, Norimatsu *et al*, Formation process of graphene on SiC(0 0 0 1), page 691. Copyright 2010 with permission from Elsevier. (b) STM current image showing graphene growth on a sidewall structure (the superimposed profile represents the actual height). The sidewall and the upper region have a honeycomb structure; the bottom part does not. (c) Cross-sectional TEM image showing overgrowth. The inset shows more graphene layers on the sidewall (highlighted by lines), indicating that the growth starts in this region.

conditions where graphene forms on the facet but not yet on the plateau (figure 8(b)).

A STM shows the characteristic honeycomb of graphene on the sidewall. Because of slight ribbon overgrowth, some graphene is also visible on the top plateau but none is seen at the bottom of the etched trench. This indicates that the growth starts at the facet. Upon further annealing (figure 8(c)) four graphene layers have grown on the sidewall and a monolayer graphene extends everywhere else, confirming a crystallographic face-dependent growth rate. These growth studies thus confirm that SiC step flow produces the facets and that graphene nucleation occurs preferentially on the facets until
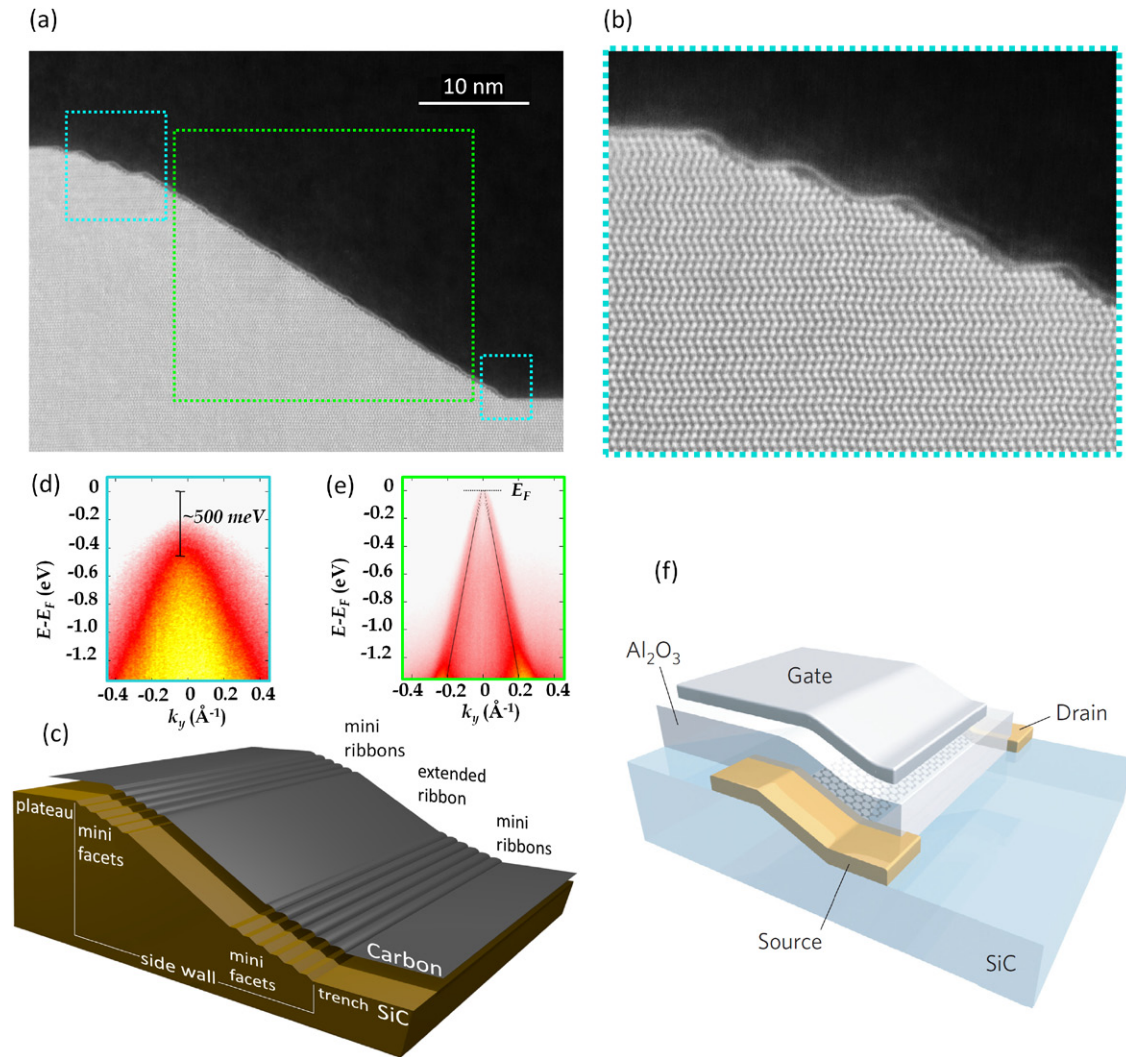
Figure 9. Epitaxial growth of graphene on SiC sidewalls. (a) Cross-section TEM image of a sidewall graphene structure. The blue rectangle indicates a region with 1–2 nm mini-ribbons on top of the existing mini-facets on SiC. The green rectangle in (a) indicates an extended ribbon on the SiC(1$\bar{1}$07) facet. (b) Zoom of the upper rectangle in (a) showing graphene floating above the facet and anchored on the plateaus. (c) Model of graphene grown on a sidewall structure. (d) Band gap opening $E_F - E_{VB} \sim > 500$ meV for mini-ribbons measured by ARPES in the lateral rectangles in panel (a). (e) Electronic band structure of neutral graphene on the main facet (central rectangle in panel a) probed by ARPES [76, 77]. Reprinted with permission from Palacio *et al* [76]. Copyright 2015 by the American Chemical Society. Reprinted with permission from Macmillan Publishers Ltd: Nature Physics 9, 49. Copyright 2012. (f) Complete transistor using the sidewall ribbon as the conduction channel and provided with source, drain and a top gate. More than 10 000 transistors have been produced at once [78]. Reprinted with permission from Macmillan Publishers Ltd: Nature Nanotechnology 5, 727. Copyright 2010.

enough layers grow to finally form a continuous topmost layer [74, 79, 80].

A side-view of a Gr/SiC sidewall system is shown in figures 9(a) and (b). The plateau and trench correspond to the SiC(0 0 0 1) surface. The central part of the sidewall has a [1 $\bar{1}$ 0 7] normal and angle-resolved photoemission spectroscopy (ARPES) measurements (figure 9(e)) show the conical graphene band structure with nearly zero doping. Where the facet merges into the flat SiC(0 0 0 1) surfaces, at the top and bottom, the facet subdivides into mini-facets. A continuous graphene layer wraps the central part as well as the mini-faceted regions [76]. The width of the large ribbon can be tuned depending on the initial lithographic trench depth. It is these sidewall ribbons that show ballistic transport [2]. Each subfacet is limited laterally by (0 0 0 1) terraces onto

which graphene is tightly bound. The mini-facets are narrow enough ($\sim$1–2 nm) that the graphene on them experiences significant quantum confinement. The location of the mini-facets (blue squares in figures 9(a) and (b)) is consistent with the angular region where a large gap was observed in ARPES [76, 77]. Large-scale integration of field effect transistors based on similarly produced ribbons (but on the (0 0 0 -1) C-terminated face) was demonstrated, as shown in figures 9(c) and 14(d), where a density of 10 000 transistors in 0.24 cm^2 was realized [81].

4. Edge stability and edge states

Edge stability is an important aspect of nanoribbons if their electronic properties are to be tailored. In armchair ribbons,
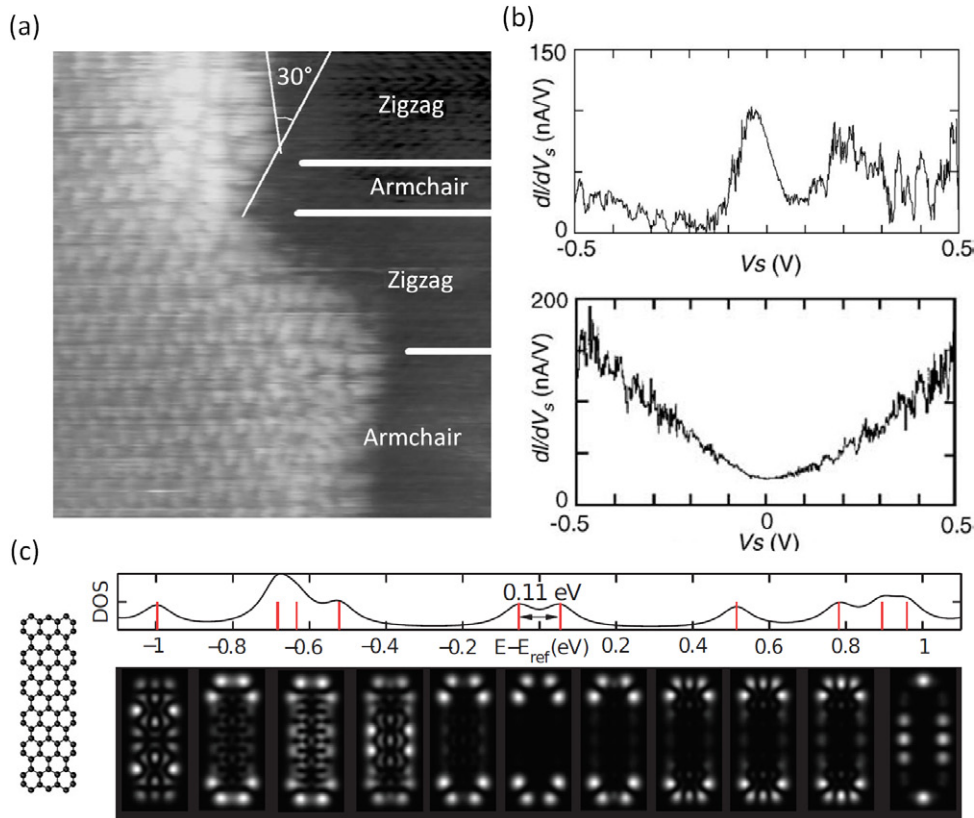
Figure 10. Edge states as a function of the edge orientation. (a) STM image showing a mixture of edges on graphite HOPG. (b) dI/dV spectra showing an edge state peak in the DOS for zigzag edges (top) and no peak for armchair edges (bottom) [82]. Reprinted from Physica E: Low-dimensional Systems and Nanostructures, vol. 34, page 678, copyright 2006, with permission from Elsevier. (c) Calculated DOS for a finite ribbon and simulated dI/dV maps at different energies for an s-wave tip [83]. Reprinted figure with permission from Ijäs *et al* [83]. Copyright 2013 by the American Physical Society.

the theoretical gap is inversely proportional to the width. In zigzag ribbons tight-binding calculations predict metallic edge states [19, 20, 49, 82]. This expected behaviour was observed by a STM on a step edge of HOPG, see figure 10(a) where both armchair and zigzag orientations are shown. Scanning tunnelling spectroscopy (STS) performed on both terminations confirms the presence of edge states on zigzag but not on armchair edges (figure 10(b)). These measurements are consistent with DFT simulations for a finite armchair graphene nanoribbon, where the DOS is plotted versus the energy (figure 10(c)). In the calculation, at $E = 0$, the armchair edges of the ribbon have a zero DOS, whereas a non zero DOS is located at the zigzag regions (figure 10(c)).

Edge states are observed by STS in ribbons obtained by opening SWCNTs [49]. Figure 11 shows the spectra along the parallel and perpendicular directions to the edge of a ribbon with an edge different from a zigzag or armchair orientation (chiral). Peaks in the spectra correspond to states located at the ribbon edge. Periodic oscillations in the peak amplitude are observed along the ribbon edge, correlated to the structural periodicity of the edge. The splitting of the peaks is attributed to spin-polarization of the edge as expected from theory [26, 27, 29]. In light of this structural dependence, the question of ribbon edge stability is relevant. [84]. In the case of sidewall ribbons, the situation is more complex because the epitaxial ribbon characteristics depend on the substrate morphology the

ribbon grows onto. Under certain growth conditions, the zigzag SiC sidewalls tend to undergo a multi-faceting, leading to zigzag trenches less straight than the armchair sidewall as seen in the STM three-dimensional representations in figure 12. This tendency for zigzag SiC facets to be less stable is further confirmed by low energy electron microscopy (LEEM), micro-low energy electron diffraction (μ-LEED), x-ray photoelectron emission microscopy (XPEEM) and μ-ARPES measurements [85].

4.1. Summary of ribbons and preparations

Band gaps can be determined unambiguously by spectroscopic measurements, either optical absorption or electronic structure measurements. The latter include STS, a combination of photoemission spectroscopy (PES) and inverse photoemission spectroscopy (IPES). Photoemission can determine the band gap when the Fermi energy is placed in the conduction band. Otherwize, when the Fermi level is somewhere within the band gap, photoemission gives a minimum value of the gap. Photoemission requires ripple-free and homogeneous areas for such determinations. STS has the advantage of being an atomic scale measurement, but does not probe the ribbon as a whole as is done in transport measurements.

Transport measurements in general cannot distinguish between a vanishing conductance due to a true band gap (i.e. no states available) and a mobility gap due to localization
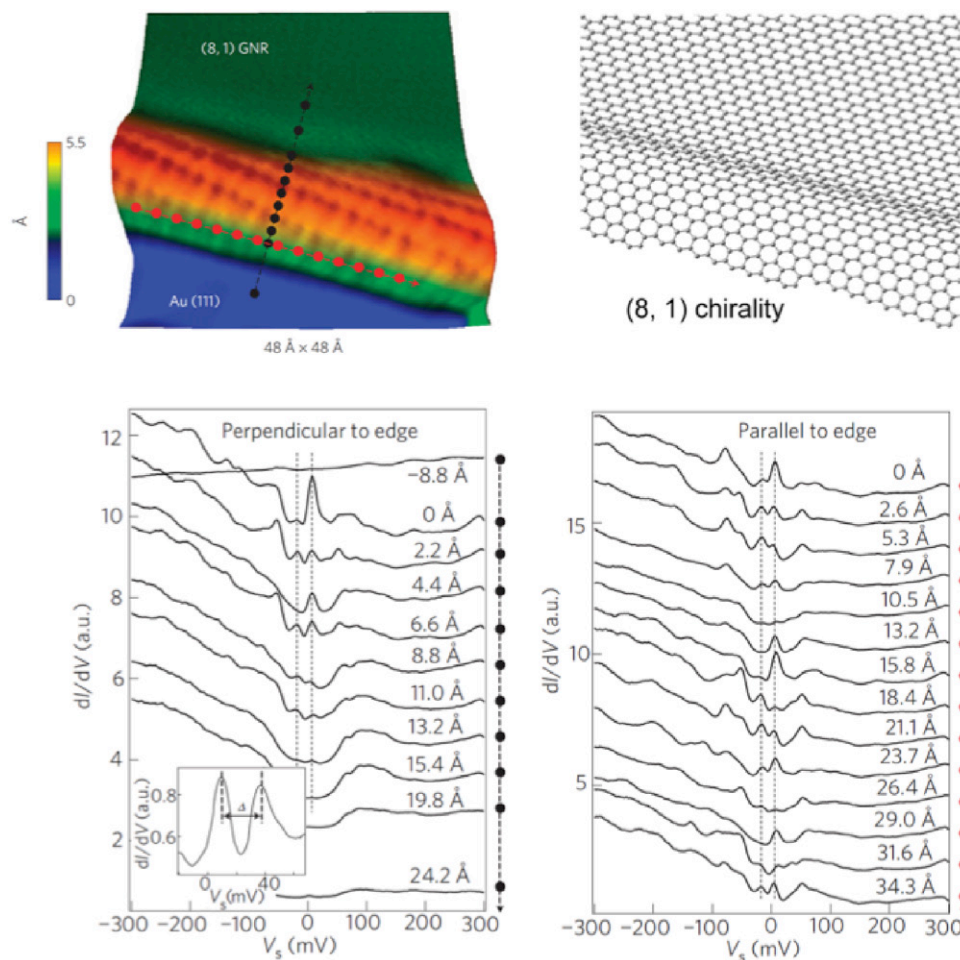
J. Phys. D: Appl. Phys. 49 (2016) 143001

Topical Review

Figure 11. Edge states in a chiral ribbon fabricated by unzipping a CNT. Top panel: STM image of the ribbon and schematics of the edge. Lower panel: dI/dV curves measured in the direction parallel (red dots) and perpendicular to the edge (black dots). The oscillatory behaviour of the peak intensity correlates with the structural periodicity of the edge. [49] Reprinted with permission from Macmillan Publishers Ltd: Nature Physics 7, 616. Copyright 2011.
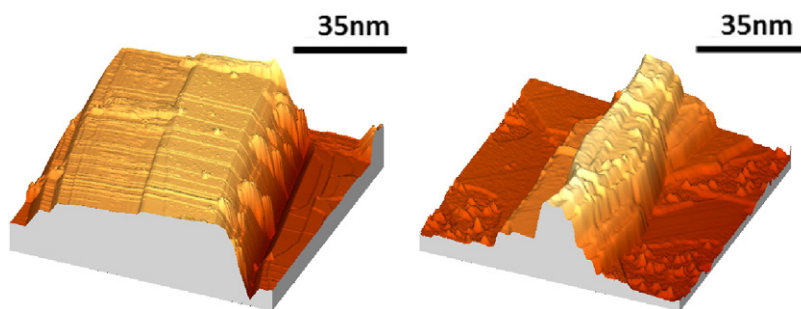

Figure 12. Stability of SiC sidewall facets with graphene grown on them. Three-dimensional view of STM images of armchair sidewall (left) and zigzag sidewall (right).

effects (i.e. presence of non-conducting states). Very detailed low-temperature transport data analysis is required for that. In both cases, a vanishing conductance at low-bias voltage and a strong conductance increase with gate and bias voltages (i.e. large current on/off ratios) are expected, and these effects depend strongly on temperature. In most ribbons produced in the literature, and especially lithographically-patterned nanoribbons, defects associated with edge roughness and the inhomogeneous potential created by impurities create a series of interconnecting quantum dots (figure 13(a)) [86, 88–90].

The overall effect of this potential is the onset of a 'transport gap', due to localization effects and Coulomb charge blocking. This means that the conductance drops to zero around the charge-neutrality point even in the absence of a true band gap. Figure 13(b) shows the conductance as a function of bias for a graphene nanoribbon exhibiting a transport gap in the region of gate voltage ΔV_g. When the gapped region is analysed more carefully (see the inset), small resonant conductance peaks can be seen. This gap is often inversely proportional to the width (figure 13(c)) [38, 86, 87, 91], which makes it more difficult
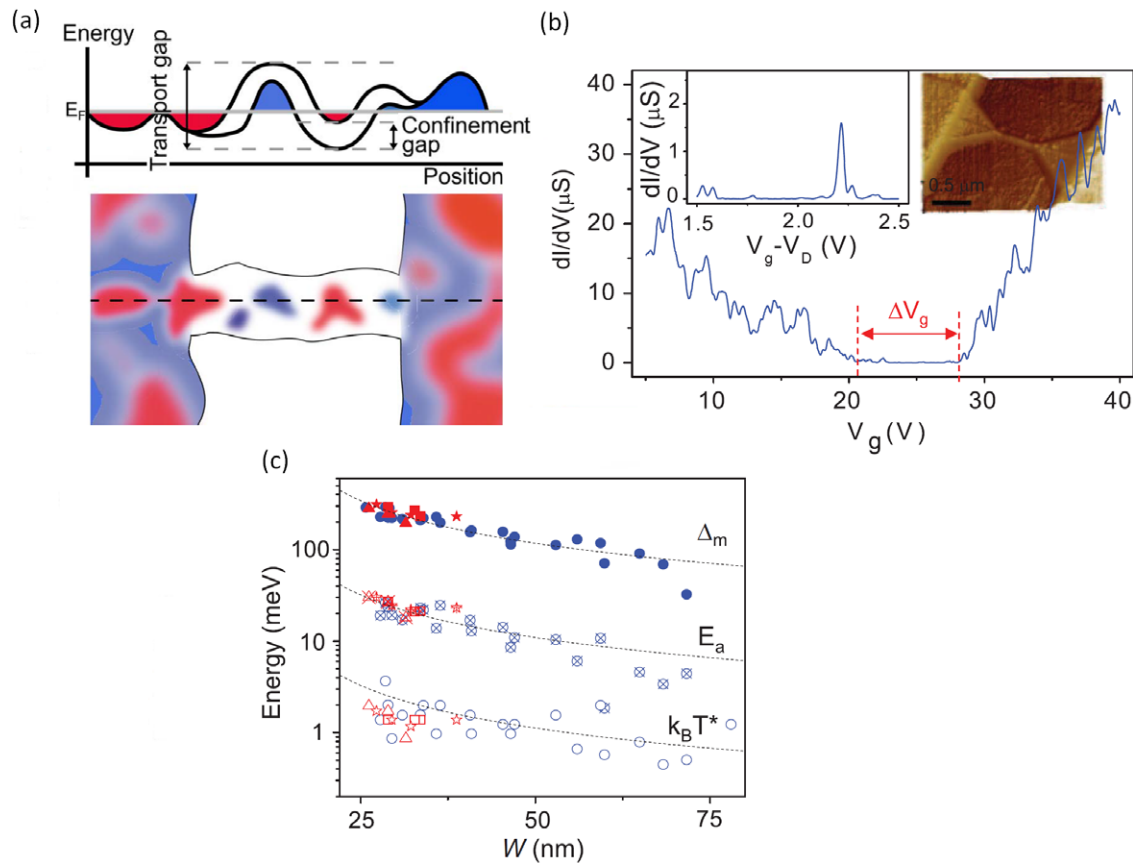
Figure 13. (a) Schematics of quantum dots created along a graphene nanoribbon creating a transport gap. The profile along the channel shows the comparison of the transport and the confinement gap [86]. Reprinted figure with permission from Gallagher *et al* [86]. Copyright 2010 by the American Physical Society. (b) Conductance (dI/dV) as a function of back-gated voltage (V_g) near the charge neutrality point showing the transport gap region. Left inset: conductance peak present on the transport gap region. Right inset: AFM image of the graphene nanoribbon channel [87]. (c) Three energetic indicators (Δ_m—energy in the single particle energy spectrum, E_a—hopping energy, $k_B T$—characteristic temperature for activated transport) for the transport gap are plotted versus the width and length of ribbons, where each symbol represents a different length of ribbon [87]. Reprinted figure with permission from Han *et al* [87]. Copyright 2010 by the American Physical Society.

to unravel a possible true band gap. Recently 10 nm wide epitaxial graphene ribbon arrays have been produced on SiC by careful standard lithographic methods, and transport data are analysed with a classical picture of a 140 meV band gap [45], which may put lithographic methods back into the game.

Keeping these distinction of the measurement of the gap in mind, published gap values, on/off ratios, resistances and mobilities for ribbons prepared with different processes are listed in tables 1 and 2. The listed gaps are transport gaps (mostly at cryogenic temperature), unless otherwize specified.

5. Devices

Devices need a real band gap and not a transport one. The fact that homogeneous smooth-edged nanoribbons are necessary to prevent localization effects was the main motivation for the development of epitaxial graphene sidewall ribbons. These are grown directly at high temperature on sidewall templates, so that the edges are well annealed and reach their state of minimal energy, terminating either in SiC or seamlessly into the buffer layer. Figure 14(a) shows STM images of graphene as it drapes

over the sidewall. The central panels correspond to the graphene ribbon on the main facet. STS curves show the absence of a band gap on the ribbon. On both sides of the ribbon, the zigzag edges are identifiable (central row panels). On the flat plateau and trench bottom (top row, left and right panels, respectively), the graphene is tightly bound to SiC and a superperiodicity is observed. The corresponding semiconducting STS curves in these regions confirm the presence of the buffer layer. This also indicates that non-gaped graphene (i.e. graphene nanoribbon) is limited to the sidewall. Remarkably these graphene nanoribbons, not only have no band gap (as seen in STS, figure 14, and ARPES, figure 9), but they are room temperature ballistic conductors over distances up to 16 μm. Figure 14(b) shows resistance measurements of epitaxial graphene nanoribbons as a function of the spacing between the probes. The resistance as a function of length extrapolates to a single conductance quantum (=1/27 kΩ^{-1}) a zero length. For a diffusive channel, the resistance would be zero. The very small length dependence corresponds to mean-free paths much longer than the ribbon length. This establishes the ballistic behaviour [2]. Ballistic transport is also observed for curved ribbons, with no particular orientation [2]. These exceptional results are not fully understood, but demonstrate that well-prepared graphene

Table 1. Band gap and structural properties.

	Fabrication methods	Orientation	Width (nm)		Gap (meV)	
Top–down	Conventional lithography	Not specified	4–500	[18, 31, 32, 36], [38–43] [35, 71, 86–89, 94]	4–500	[31, 36, 38] [41, 89]
	Local probe lithography	Not specified	0.7–12	[34, 51]	100–500	[33, 51]
		AC	2.5	[33]		
	Chemical	Not specified	3–300	[47, 54, 95]	10–400	[54]
	Unzipping CNTs	Not specified	10–300	[57–60, 96, 97]	10–50	[49, 57]
		Chiral	80–200	[49]		
	Particle cutting	Not specified	>10	[64, 65]	120–1600	[98]
		ZZ	>1.1	[63, 98]		
Bottom–up	Molecular precursor-based	AC	0.7–13	[66, 67, 68, 99, 87]	1300–3100	[46, 56, 67]
		ZZ	1	[56]		[68, 87–92]
	CVD	Not specified	20–3000	[70, 72, 73]	50–58.5	[70, 72]
	Epitaxial graphene	Not specified	900	[100]	—	
Epi	Epitaxial sidewall	ZZ	40	[2, 101]	—	
		AC	2–40	[76, 77, 81]	>500	[76]

Notes: Listed gap values are either transport gaps or band gaps. True band gaps are listed for local probe lithography (STS measurements [33, 51]), and molecular precursor (PES-IPES [46, 67], optical absorption [56], STS [39, 92]) and unzipping CNTs (STS [49]) and epitaxial graphene (ARPES [76, 93]). All others are transport measurements.

Table 2. Reported on/off ratio and transport properties for ribbons prepared with various processes.

	Fabrication methods	On/Off ratio		Resistance (KΩ)		Mobility $(\text{cm}^2\,(\text{V·s})^{-1})$	
Top–down	Conventional lithography	5–1000 RT	[31, 42] [71, 41]	30–670	[36]	0.21–6000	[36, 86] [42, 71]
	Local probe lithography	—	[34]	100	[34]	—	[34]
	Chemical	10^7 RT	[54]	—	[54]	100–200	[54]
	Unzipping CNTs	10–100 RT	[59]	2	[57]	0.1–1500	[57, 59] [97]
Bottom–up	Molecular precursor-based	—		—		150–150 000	[56]
	CVD	2–15 000 RT, LT	[70, 72] [73]	100	[73]	40–1000	[70, 72] [73]
	Epitaxial graphene	$5 \cdot 10^6$ RT	[45, 100]	10	[100]	10–1000	[45, 100]
Epi	Epitaxial sidewall	—		7–26	[101, 81] [2]	2700 Ballistic	[81] [2]

Notes: RT (LT, respectively) refers to room temperature (cryogenic, respectively) measurements.

nanoribbons bear a strong resemblance to CNTs [102], which are edgeless but for which chirality determines the electronic structure.

Integration of ribbons into devices has followed several directions, but all require junctions and heterojunctions. An example of an all-graphene np junction was obtained by assembling different molecular precursors, connecting graphene ribbons with p- or n-doping in a continuous graphene ribbon [92], as shown in figure 15(a). Another example is epitaxial graphene, where the intercalation of one or two layers of Ge below the graphene layer changes the graphene doping from n to p respectively, creating small junctions (see figure 15(b)) [103]. Although the intercalation is not very well controlled at this point it provides an easy route to reversible doping. Epitaxial graphene also provides conducting graphene to semiconducting junctions. For instance the band-gapped region at the top of the curved sidewall graphene ribbon is seamlessly connected to a conducting facet making it an all graphene semiconductor-conductor junction [76, 77]. In another instance, two-dimensional graphene was used as integrated leads in SiC semiconducting devices connecting a SiC channel [104] or an atomically thin SiC/Si_2O_3 channel [100].

Other devices integrating graphene nanoribbons include sensors [105, 106] or photodetectors [61, 107–109]. Figure 16 shows some of the integration of graphene nanoribbons in electronic devices. Figure 16(a) presents a suspended graphene
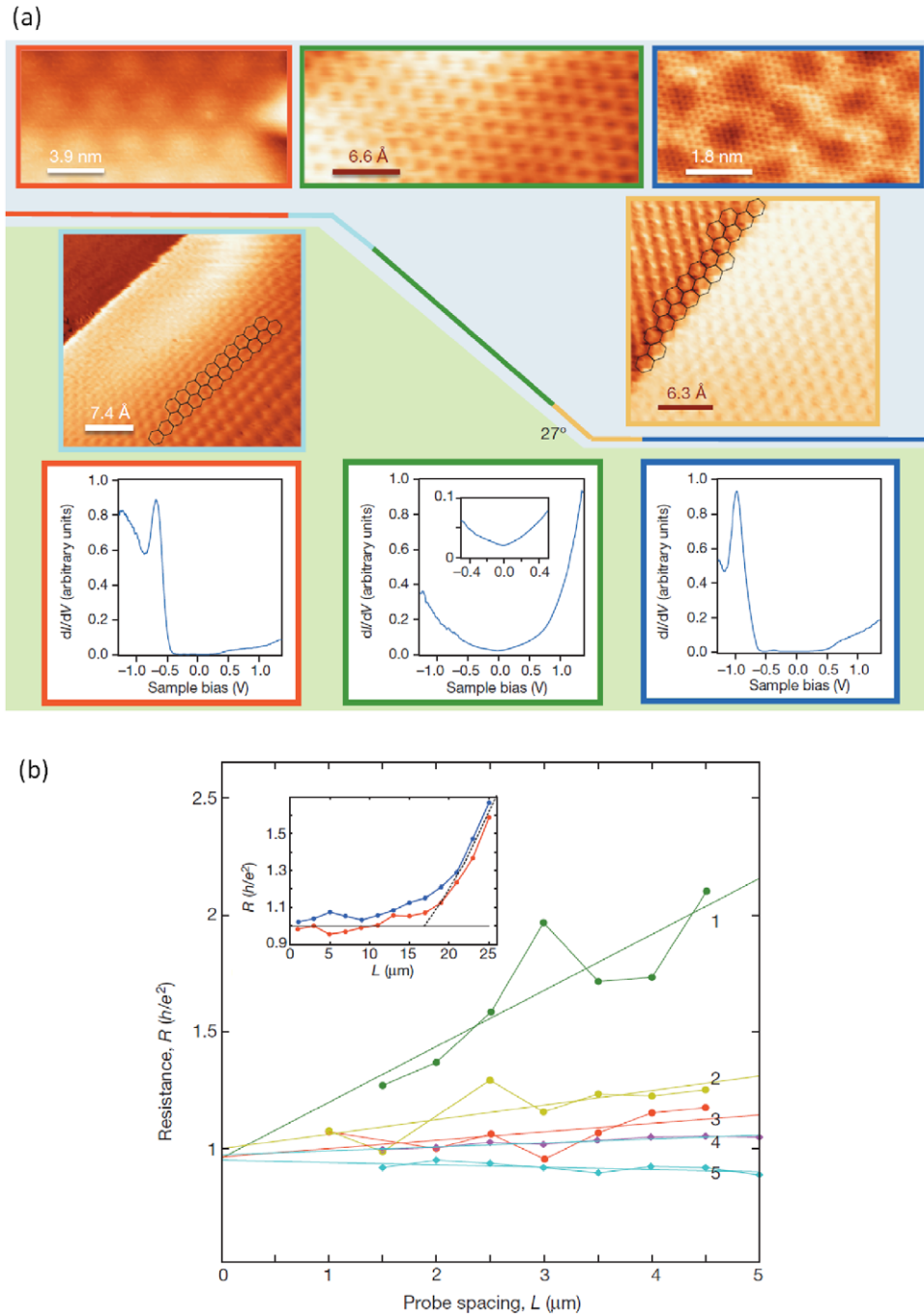
Figure 14. Ballistic transport of sidewall nanoribbons. (a) Schematic and corresponding STM images and STS spectra for a sidewall graphene nanoribbon structure. The central panel corresponds to the ribbon on the main facet, while the plateau and the bottom trench are on the left and right, respectively. The dI/dV curve shows a zero band-gap signature of graphene for the nanoribbon, while the plateau and trench are the semiconducting buffer layer. (b) Resistance measurement of a sidewall graphene nanoribbon at different probing lengths (L). 1 is a sample prepared *ex situ*, 2–5 are for successive annealings on a ribbon grown *in situ*. The resistance extrapolates at 1 conductance quantum ($e^2 \, h^{-1}$) at zero length, and varies little with length, indicating ballistic transport. The inset shows that the resistance is constant up to 16 μm [2] (reprinted with permission from Macmillan Publishers Ltd: Nature 506, 394. Copyright 2014.)

nanoribbon connected to multiple source-drain electrodes to measure its electronic properties. The electron beam of a TEM was used to nanosculpture the suspended ribbon into various widths so as to change its electronic properties [34]. Figure 16(b) shows conventional lithography patterning on graphene flakes to obtain nanoribbons with different widths. Electrical measurements are possible due to the Pd source-drain contacts, back-gated on the substrate. Figure 16(c)–(d) show examples of

graphene nanoribbons showing the feasibility of the production of large device networks. Field-effect transistor (FET) devices have also been demonstrated [110–114]. Figure 16(c) shows a 50-FET array where CVD was used to grow the graphene nanoribbons vertically along with four-contact electrodes on each ribbon (red inset) [72]. Finally, figure 16(d) shows a transistor array on graphene sidewall nanoribbons. With this method 40 000 devices per cm^2 were produced [78].
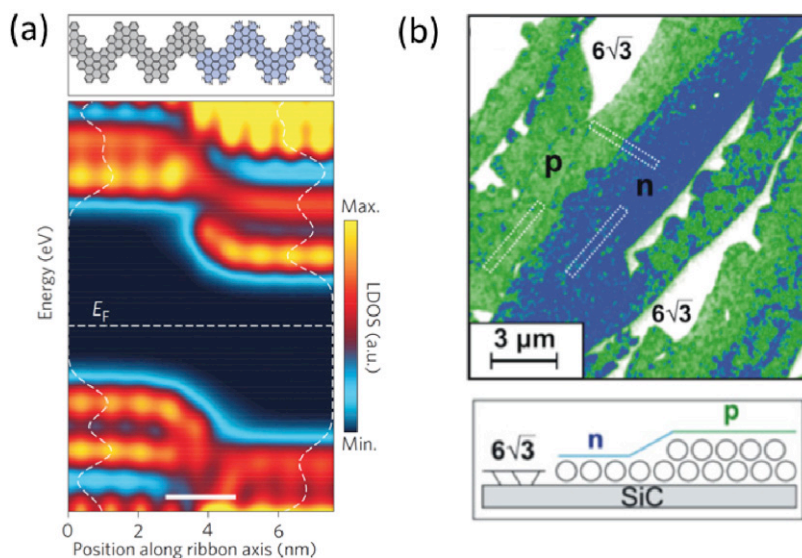
Figure 15. All graphene pn junctions. (a) Schematics of a graphene theoretical heterojunction, where the left part is p-doped and the right part is n-doped. Below the LDOS along the ribbon axis, as calculated by DFT calculations allows to visualize the pn junction [92] (reprinted with permission from Macmillan Publishers Ltd: Nature Nanotechnology 9, 896. Copyright 2014. (b) Colour-coded SEM image of the n-(blue) and p-(green) doped areas obtained by the intercalation of one (two, respectively) layer of Ge at the interface between SiC and epitaxial graphene, as sketched in the bottom panel [103]. Reprinted with permission from Baringhaus *et al* [103]. Copyright 2014 by the American Chemical Society.
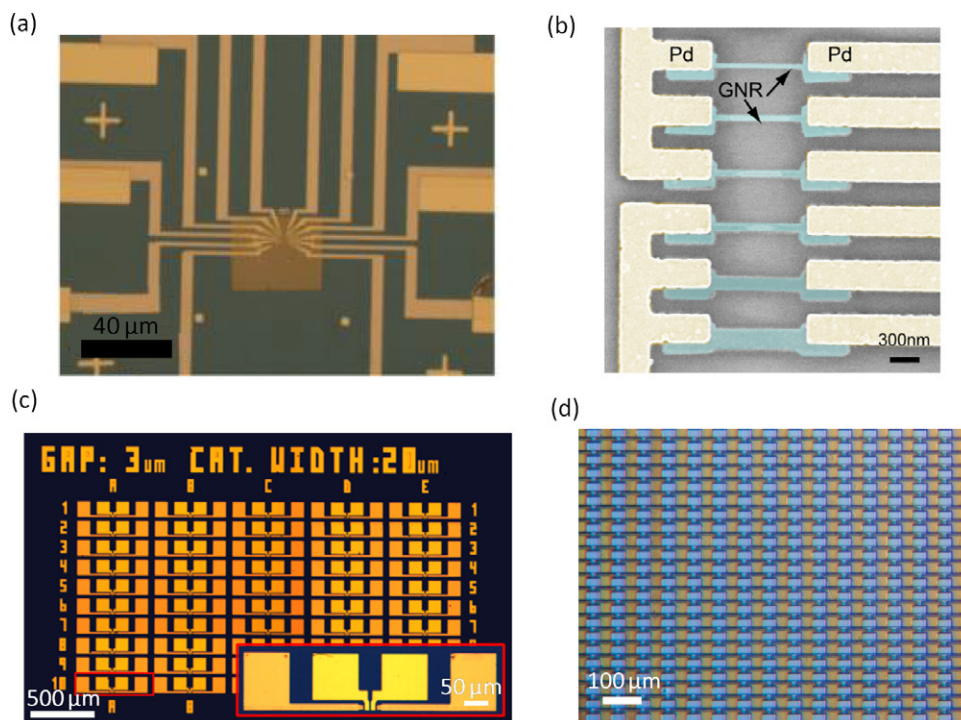

Figure 16. Devices. (a) A chip with multiple electrodes connected to a suspended graphene nanoribbon obtained by TEM lithography [34]. Reprinted with permission from Qi *et al* [34]. Copyright 2014 by the American Chemical Society. (b) FET device obtained by e-beam lithography patterning. The graphene nanoribbons are contacted by Pd electrodes [36]. Reprinted from Physica E: Low-dimensional Systems and Nanostructures, vol. 40, Chen *et al* Graphene nano-ribbon electronics, 5, Copyright 2007, with permission from Elsevier. (c) A 50 graphene nanoribbons FET array developed from CVD graphene on a catalyst template. The inset shows the four-electrode contact configuration [72]. Reprinted with permission from Martin-Fernandez *et al Nano Lett.* **12** 6175. Copyright 2012 by the American Chemical Society. (d) Optical image of a transistor array of graphene nanoribbons on SiC(0 0 0 1) sidewalls. Device density scales up to 40 000 per cm^2 [78]. The individual transistor is shown in figure 9(f). Reprinted with permission from Macmillan Publishers Ltd: Nature Nanotechnology 5, 727. Copyright 2010.

6. Conclusions and perspectives

The current review shows that a large research effort was dedicated to graphene nanoribbon production and measurements. The driving force was to create a band gap by electronic confinement in gapless graphene. If lithographically-patterned ribbons seem to be plagued with rough edges and associated localization effects, promising results are shown from ribbons produced directly into shape. These include notably the chemical assembly of molecules and epitaxial graphene sidewall ribbons on SiC. In both cases, the ribbon orientation is controlled and the edges are well terminated. Benchmark results were demonstrated with a eV-wide band gap in sub-nm wide chemically-assembled armchair ribbons. The half-eV band gap from the ARPES measurement is associated with a 1-2nm wide epitaxial graphene sidewall ribbon. Remarkably gapless sidewall ribbons are room temperature single channel ballistic conductors. How these graphene nanostructures may find their way into real-life applications is still a work in progress, but the potential of graphene-directed growth with a clean industrial scalable process has been demonstrated.

Acknowledgments

References

[1] Berger C *et al* 2004 *J. Phys. Chem.* B **108** 19912
[2] Baringhaus J *et al* 2014 *Nature* **506** 394
[3] Wong J-H, Wu B-R and Lin M-F 2012 *J. Phys. Chem.* C **116** 8271
[4] Pereira V, Castro Neto A and Peres N 2009 *Phys. Rev.* B **80** 045401
[5] Levy N, Burke S A, Meaker K L, Panlasigui M, Zettl A, Guinea F, Neto A H C and Crommie M F 2010 *Science* **329** 544
[6] Li M, Wang L, Yu N, Hou T and Li Y 2015 *J. Mater. Chem.* C **3** 3645
[7] Balog R *et al* 2010 *Nat. Mater.* **9** 315
[8] Castellanos-Gomez A, Wojtaszek M, Arramel A, Tombros N and van Wees B 2012 *Small* **8** 1607
[9] Luo Z, Shang J, Lim S, Li D, Xiong Q, Shen Z, Lin J and Yu T 2010 *Appl. Phys. Lett.* **97** 233111
[10] Matis B, Burgess J, Bulat F, Friedman A, Houston B and Baldwin J 2012 *ACS Nano* **6** 17
[11] Bekyarova E, Itkis M, Ramesh P, Berger C, Sprinkle M, de Heer W and Haddon R 2009 *J. Am. Chem. Soc.* **131** 1336
[12] Denis P 2010 *Chem. Phys. Lett.* **492** 251
[13] Denis P 2014 *Chem. Phys. Chem.* **15** 3994
[14] Sharif Azadeh M S, Kokabi A, Hosseini M and Fardmanesh M 2011 arXiv: 1102.5422v1
[15] Zhang W *et al* 2011 *ACS Nano* **5** 7517
[16] Lv R and Terrones M 2012 *Mater. Lett.* **78** 209
[17] Biel B, Triozon F, Blase X and Roche S 2009 *Nano Lett.* **9** 2725
[18] Berger C *et al* 2006 *Science* **312** 1191
[19] Nakada K, Fujita M, Dresselhaus G and Dresselhaus M S 1996 *Phys. Rev.* B **54** 17954
[20] Wakabayashi K, Fujita M, Ajiki H and Sigrit M 1999 *Phys. Rev.* B **59** 8271
[21] Wagner P *et al* 2013 *J. Phys. Chem.* C **117** 26790
[22] Son Y W, Cohen M L and Louie S G 2006 *Nature* **444** 347
[23] Ma F, Guo Z, Xu K and Chu P K 2012 *Solid State Commun.* **152** 1089
[24] Martín-Martínez F J, Fias S, Van Lier G, De Proft F and Geerlings P 2012 *Chem.: A Eur. J.* **18** 6183
[25] Barone V, Hod O and Scuseria G 2006 *Nano Lett.* **6** 2748
[26] Son Y-W, Cohen M and Louie S 2006 *Phys. Rev. Lett.* **97** 216803
[27] Yang L, Park C-H, Son Y-W, Cohen M and Louie S 2007 *Phys. Rev. Lett.* **99** 186801
[28] Pisani L, Chan J, Montanari B and Harrison N 2007 *Phys. Rev.* B **75** 064418
[29] Yazyev O 2010 *Rep. Prog. Phys.* **73** 056501
[30] Wakabayashi K and Takane Y 2007 *Phys. Rev. Lett.* **99** 036601
[31] Bai J, Duan X and Huang Y 2009 *Nano Lett.* **9** 2083
[32] Liu G *et al* 2012 *ACS Nano* **6** 6786
[33] Tapasztó L, Dobrik G, Lambin P and Biró L P 2008 *Nat. Nanotechnol.* **3** 397
[34] Qi Z J, Rodríguez-Manzo J A, Botello-Méndez A R, Hong S J, Stach E A, Park Y W, Charlier J C, Drndić M and Johnson A T C 2014 *Nano Lett.* **14** 4238
[35] de Heer W A *et al* 2007 *Solid State Commun.* **143** 92
[36] Chen Z, Lin Y-M, Rooks M J and Avouris P 2007 *Phys. E: Low Dimens. Syst. Nanostruct.* **40** 228
[37] Sang-Chul J 2010 *Trans. Electr. Electron. Mater.* **11** 190
[38] Han M, Ozylmaz B, Zhang Y and Kim P 2007 *Phys. Rev. Lett.* **98** 206805
[39] Chen X-D, Liu Z-B, Jiang W-S, Yan X-Q, Xing F, Wang P, Chen Y and Tian J-G 2013 *Sci. Rep.* **3** 3216
[40] Gardener J A and Golovchenko J A 2012 *Nanotechnology* **23** 185302
[41] Wang X and Dai H 2010 *Nat. Chem.* **2** 661
[42] Sinitskii A and Tour J M 2012 *Appl. Phys. Lett.* **100** 103106
[43] Xu G, Bai J, Torres C M, Song E B, Tang J, Zhou Y, Duan X, Zhang Y and Wang K L 2010 *Appl. Phys. Lett.* **97** 073107
[44] Bryan S and Yang Y 2011 *J. Phys. Chem.* C **115** 10230
[45] Hwang W S *et al* 2015 *APL Mater.* **3** 011101
[46] Vo T H, Shekhirev M, Kunkel D A, Morton M D, Berglund E, Kong L, Wilson P M, Dowben P A, Enders A and Sinitskii A 2014 *Nat. Commun.* **5** 3189
[47] Wu Z, Reb W, Gao L, Liu B, Zhao J and Cheng H 2010 *Nano Res.* **3** 16
[48] Kosynkin D V, Higginbotham A L, Sinitskii A, Lomeda J R, Dimiev A, Price B K and Tour J M 2009 *Nature* **458** 872
[49] Tao C, Jiao L, Yazyev O V, Chen Y C, Feng J, Zhang X, Capaz R B, Tour J M, Zettl A and Louie S G 2011 *Nat. Phys.* **7** 616
[50] Ribeiro R, Poumirol J M, Cresti A, Escoffier W, Goiran M, Broto J-M, Roche S and Raquet B 2011 *Phys. Rev. Lett.* **107** 086601
[51] Magda G Z, Jin X, Hagymási I, Vancsó P, Osváth Z, Nemes-Incze P, Hwang C, Biró L P and Tapasztó L 2015 *Nature* **514** 608
[52] Wei Z *et al* 2010 *Science* **328** 1373
[53] Jia X *et al* 2009 *Science* **323** 1701
[54] Li X, Wang X, Zhang L, Lee S and Dai H 2008 *Science* **319** 1229
[55] Vallés C, Drummond C, Saadaoui H, Furtado C A, He M, Roubeau O, Ortolani L, Monthioux M and Pénicaud A 2008 *J. Am. Chem. Soc.* **130** 15802
[56] Narita A *et al* 2013 *Nat. Chem.* **6** 126
[57] Jiao L, Wang X, Diankov G, Wang H and Dai H 2010 *Nat. Nanotechnol.* **5** 321
[58] Shinde D B, Majumder M and Pillai V K 2014 *Sci. Rep.* **4** 4363

J. Phys. D: Appl. Phys. **49** (2016) 143001

Topical Review

[59] Jiao L, Zhang L, Wang X, Diankov G and Dai H 2009 *Nature* **458** 877

[60] Elías A L, Botello-Méndez A R, Meneses-Rodríguez D, Jehová González V, Ramírez-González D, Ci L, Muñoz-Sandoval E, Ajayan P M, Terrones H and Terrones M 2010 *Nano Lett.* **10** 366

[61] Wei D, Xie L, Lee K, Hu Z, Tan S, Chen W, Sow C, Chen K, Liu Y and Wee A 2013 *Nat. Commun.* **4** 1374

[62] Gong Y *et al* 2013 *Phys. Rev.* B **87** 165404

[63] Campos L C, Manfrinato V R, Sanchez-Yamagishi J D, Kong J and Jarillo-Herrero P 2009 *Nano Lett.* **9** 2600

[64] Ci L, Xu Z, Wang L, Gao W, Ding F, Kelly K F, Yakobson B I and Ajayan P M 2008 *Nano Res.* **1** 116

[65] Datta S S, Strachan D R, Khamis S M and Johnson A T C 2008 *Nano Lett.* **8** 1912

[66] Cai J *et al* 2010 *Nature* **466** 470

[67] Linden S *et al* 2012 *Phys. Rev. Lett.* **108** 216801

[68] Chen Y C, de Oteyza D G, Pedramrazi Z, Chen C, Fischer F R and Crommie M F 2013 *ACS Nano* **7** 6123

[69] Huang H, Wei D, Sun J, Wong S L, Feng Y P, Neto A H C and Wee A T S 2012 *Sci. Rep.* **2** 983

[70] Kato T and Hatakeyama R 2012 *Nat. Nanotechnol.* **7** 651

[71] Sokolov A N *et al* 2013 *Nat. Commun.* **4** 2402

[72] Martin-Fernandez I, Wang D and Zhang Y 2012 *Nano Lett.* **12** 6175

[73] Wang D, Tian H, Yang Y, Xie D, Ren T-L and Zhang Y 2013 *Sci. Rep.* **3** 1348

[74] Norimatsu W and Kusunoki M 2010 *Phys. E: Low Dimens. Syst. Nanostruct.* **42** 691

[75] van Bommel A, Crombeen J and van Tooren A 1975 *Surf. Sci.* **48** 463

[76] Palacio I *et al* 2014 *Nano Lett.* **15** 182

[77] Hicks J *et al* 2012 *Nat. Phys.* **9** 49

[78] Sprinkle M, Ruan M, Hu Y, Hankinson J, Rubio-Roy M, Zhang B, Wu X, Berger C and de Heer W A 2010 *Nat. Nanotechnol.* **5** 727

[79] Borovikov V and Zangwill A 2009 *Phys. Rev.* B **80** 121406

[80] Ming F and Zangwill A 2012 *J. Phys. D: Appl. Phys.* **45** 154007

[81] Sprinkle M *et al* 2010 *J. Phys. D: Appl. Phys.* **43** 374006

[82] Kobayashi Y, Kusakabe K, Fukui K and Enoki T 2006 *Phys. E: Low Dimens. Syst. Nanostruct.* **34** 678

[83] Ijäs M, Ervasti M, Uppstu A, Liljeroth P, van der Lit J, Swart I and Harju A 2013 *Phys. Rev.* B **88** 075429

[84] Liu Y, Dobrinsky A and Yakobson B 2010 *Phys. Rev. Lett.* **105** 235502

[85] Nevius M S, Wang F, Mathieu C, Barrett N, Sala A, Mentes T O, Locatelli A and Conrad E H 2014 *Nano Lett.* **14** 6080

[86] Gallagher P, Todd K and Goldhaber-Gordon D 2010 *Phys. Rev.* B **81** 115409

[87] Han M Y, Brant J C and Kim P 2010 *Phys. Rev. Lett.* **104** 056801

[88] Sols F, Guinea F and Neto A H C 2007 *Phys. Rev. Lett.* **99** 166803

[89] Stampfer C, Güttinger J, Hellmüller S, Molitor F, Ensslin K and Ihn T 2009 *Phys. Rev. Lett.* **102** 056403

[90] Oostinga J, Sacepe B, Craciun M and Morpurgo A 2010 *Phys. Rev.* B **81** 193408

[91] Gunlycke D and White C T 2010 *Phys. Rev.* B **81** 075434

[92] Cai J, Pignedoli C A, Talirz L, Ruffieux P, Söde H, Liang L, Meunier V, Berger R, Li R and Feng X 2014 *Nat. Nanotechnol.* **9** 896

[93] Hicks J, Shepperd K, Wang F and Conrad E H 2012 *J. Phys. D: Appl. Phys.* **45** 154002

[94] Xu G, Torres C M, Bai J, Tang J and Yu T 2011 *Appl. Phys. Lett.* **98** 243118

[95] Campos-Delgado J *et al* 2008 *Nano Lett.* **8** 2773

[96] Kosynkin D V, Lu W, Sinitskii A, Pera G, Sun Z and Tour J M 2011 *ACS Nano* **5** 968

[97] Zhu Y and Tour J M 2010 *Nano Lett.* **10** 4356

[98] Li Y Y, Chen M X, Weinert M and Li L 2014 *Nat. Commun.* **5** 4311

[99] Blackenburg S, Cai J, Ruffieux P, Jaafar R, Passerone D, Feng X, Müllen K, Fasel R and Pignedoli C A 2012 *ACS Nano* **6** 2020

[100] Kunc J, Hu Y, Palmer J, Guo Z, Hankinson J, Gamal S H, Berger C and de Heer W A 2014 *Nano Lett.* **14** 5170

[101] Baringhaus J, Edler F and Tegenkamp C 2013 *J. Phys.: Condens. Matter* **25** 392001

[102] Frank S, Poncharal P, Wang Z and de Heer W 1998 *Science* **280** 1744

[103] Baringhaus J, Stohr A, Forti S, Krasnikov S A, Zakharov A A, Starke U and Tegenkamp C 2014 *Appl. Phys. Lett.* **104** 261602

[104] Hertel S, Waldmann D, Jobst J, Albert A, Albrecht M, Reshanov S, Schoner A, Krieger M and Weber H 2012 *Nat. Commun.* **3** 957

[105] Johnson J, Behnam A, Pearton S and Ural A 2010 *Adv. Mater.* **22** 4877

[106] Traversi F, Raillon C, Benameur S, Liu K, Khlybov S, Tosun M, Krasnozhon D, Kis A and Radenovic A 2013 *Nat. Nanotechnol.* **8** 939

[107] Freitag M, Low T, Zhu W, Yan H, Xia F and Avouris P 2013 *Nat. Commun.* **4** 1951

[108] Shi S, Xu X, Ralph D and McEuen P 2011 *Nano Lett.* **11** 1814

[109] Ryzhii V, Ryabova N, Ryzhii M, Baryshnikov N, Karasik V, Mitin V and Otsuji T 2012 *Opt. Electron. Rev.* **20** 15

[110] Schwierz F 2013 *Proc. IEEE* **101** 1567

[111] Liu Y, Zhang L, Brinkley M, Bian G, Miller T and Chiang T-C 2010 *Phys. Rev. Lett.* **105** 136804

[112] Liu W, Jackson B, Zhu J, Miao C, Chung C, Park Y, Sun K, Woo J and Xie Y 2010 *ACS Nano* **4** 3927

[113] Ryzhii V, Ryzhii M, Satou A and Otsuji T 2008 *J. Appl. Phys.* **103** 094510

[114] Mohamadpour H and Asgari A 2012 *Phys. E: Low Dimens. Syst. Nanostruct.* **46** 270